International Journal of Radiation Oncology biology • physics

www.redjournal.org

Novel Imaging for Treatment Planning

Personalized Anatomic Eye Model From T1-Weighted Volume Interpolated Gradient Echo Magnetic Resonance Imaging of Patients With Uveal Melanoma

Huu-Giao Nguyen, PhD,[*,†,‡,§] Raphael Sznitman, PhD,[†] Philippe Maeder, MD,[‡] Ann Schalenbourg, MD,[¶] Marta Peroni, PhD,[*] Jan Hrbacek, PhD,[*] Damien C. Weber, MD,[*] Alessia Pica, MD,[*] and Meritxell Bach Cuadra, PhD[‡,§,||]

Proton Therapy Center, Paul Scherrer Institut, ETH Domain, Villigen, Switzerland; †Ophthalmic Technology Laboratory, ARTORG Center of the University of Bern, Bern, Switzerland; ‡Radiology Department, Lausanne University Hospital, Lausanne, Switzerland; §Medica Image Analysis Laboratory, Centre d'Imagerie BioMédicale, University of Lausanne, Lausanne, Switzerland; ||Signal Processing Laboratory, Ecole Polytechnique Fédérale de Lausanne, Lausanne, Switzerland; and ¶Adult Ocular Oncology Unit, Jules-Gonin Eye Hospital, FAA, Department of Ophthalmology, University of Lausanne, Switzerland

Received Jan 3, 2018, and in revised form Apr 6, 2018. Accepted for publication May 1, 2018.

Summary

We created a 3-dimensional patient-specific eye model from a T1-weighted 1.5T magnetic resonance imaging dataset of 37 subjects consisting of healthy eyes and eyes of uveal melanoma patients for integration into proton radiation treatment planning. Despite motion and bias field artifacts, our active shape model shows high levels of segmentation accuracy, even in the

Purpose: We present a 3-dimensional patient-specific eye model from magnetic resonance imaging (MRI) for proton therapy treatment planning of uveal melanoma (UM). During MRI acquisition of UM patients, the point fixation can be difficult and, together with physiological blinking, can introduce motion artifacts in the images, thus challenging the model creation. Furthermore, the unclear boundary of the small objects (eg, lens, optic nerve) near the muscle or of the tumors with hemorrhage and tantalum clips can limit model accuracy.

Methods and Materials: A dataset of 37 subjects, including 30 healthy eyes of volunteers and 7 eyes of UM patients, was investigated. In our previous work, active shape model was successfully applied to retinoblastoma eye segmentation in T1-weighted 3T MRI. Here, we evaluate this method in a more challenging setting, based on 1.5T MRI acquisition and different datasets of awake adult eyes with UM. The lens and cornea together with the sclera, vitreous humor, and optic nerve were automatically segmented and validated against manual delineations of a senior ocular radiation oncologist, in terms of the Dice similarity coefficient and Hausdorff distance.

Reprint requests to: Huu-Giao Nguyen, PhD, ARTORG Center Ophthalmic Technology Lab, Murtenstrasse 50 CH-3008, Bern, Switzerland. Tel: +41 31 632 76 12; E-mail: huu.nguyen@artorg.unibe.ch

Conflict of interest: none.

Acknowledgments—This work is funded by the Swiss Cancer Research foundation (grant no. GAP-CRG-201602). It is also supported by the Center of Biomedical Imaging of Geneva-Lausanne Universities and EPFL, the Fondation Leenaards and Fondation Louis-Jeantet.

Int J Radiation Oncol Biol Phys, Vol. 102, No. 4, pp. 813–820, 2018
0360-3016/$ - see front matter
https://doi.org/10.1016/j.ijrobp.2018.05.004

presence of tumor and tantalum clips. The lens, vitreous humor, optic nerve and sclera (combined with the cornea), vitreous humor, and optic nerve were automatically segmented and validated against manual delineations by a senior radiation oncologist.

Results: Leave-one-out cross validation (mixing both volunteers and UM patients) yielded median Dice similarity coefficient values (respective of Hausdorff distance) of 94.5% (1.64 mm) for the sclera, 92.2% (1.73 mm) for the vitreous humor, 88.3% (1.09 mm) for the lens, and 81.9% (1.86 mm) for the optic nerve. The average computation time for an eye was 10 seconds.

Conclusions: To our knowledge, our work is the first attempt to automatically segment adult eyes, including patients with UM. Our results show that automated active shape model segmentation can succeed in the presence of motion, tumors, and tantalum clips. These results are promising for inclusion in clinical practice.

Introduction

Uveal melanoma (UM) is the most common primary intraocular malignancy in the white adult population, making up 79% to 88% of primary intraocular cancers. The incidence of UM has remained stable for the last 50 years (1, 2). Many therapeutic options (3) for UM are available in ophthalmology specialized centers, including, for example, enucleation, local resection, and brachytherapy, as well as external beam radiation therapy. Since the 1970s, proton therapy (PT) has emerged as the standard of care for the vast majority of malignant melanomas of the uveal tract. PT achieves high rates of local tumor control with acceptable ocular morbidity due to intrinsic physical properties of protons, whereby the dose deposition occurs at the target tissue while relatively sparing nearby structures (4). Current clinical practice includes the need for a surgical implant of tantalum clips for tumor localization, an invasive procedure that is essential for planning and positioning. Currently, EYEPLAN software is the most widely used model-based treatment planning system for ocular PT. This software relies on a spheroidal eye model, which is adapted to the patient's eye length and clip positions. Only the location of organs at risk with respect to target are modeled, as the system does not support modern 3-dimensional (3D) imaging for the target or organs at risk definition. There is hence a need to create personalized PT planning, allowing for the localization and segmentation of eye structures. The automation of such a process would also be beneficial to reduce interobserver variability in boundary definitions, especially in posterior tumors with hemorrhage and tantalum clips.

Ocular magnetic resonance imaging (MRI) provides a large amount of information about the eye anatomy and the tumor compared with traditional A- and B-scan ultrasound given its high spatial resolutions, multiplanar capabilities, and high intrinsic contrast. This can be achieved with conventional head coils or surface coils (5-7). The predominant MRI signal is from the aqueous and vitreous humor (VH), which have more than 98% water content, resulting in a bright T2 signal and low T1 signal relative to the extraocular muscles. This specific characterization helps the differential diagnosis and follow-up monitoring owing to its contributions to the construction of 3D UM patient-specific eye models. In clinical practice, however, ocular MRI acquisition can be challenging, in particular for patients with compromised vision.

Patients are asked to fixate on a point during the entire acquisition, reducing but not fully excluding motion artifacts in the image. In addition, the presence of large amounts of fat within the orbit, poor contrast, and the small size of the eye anatomy (including tumors and clips) located near muscles can be challenging for an automatic segmentation algorithm. Figure 1a shows an example of T1-weighted vibe 1.5T MRI (with surface loop coil) of a patient with UM. Figure 1b illustrates the presence of the motion (yellow arrow) and the tumor (red arrow). Figure 1c shows an example of a 3D UM patient-specific eye model: the sclera (CS) (red), lens (green), VH (white), optic nerve (pink), tumor (blue), and clips (yellow).

The aim of this study is to improve PT planning by integrating a patient 3D MRI and its derived patient-specific eye model. Our goal is the inclusion of patient-specific 3D eye structures and the tumor shape not only for a better dose distribution but also for the standardization of the segmentation procedure. Achieving this goal would reduce both the time needed and the variability observed in manual delineations, which necessitate careful checking of semiautomated procedures, especially for poor contrast image or small eye anatomy structures (Fig. 2).

Some works have addressed the segmentation of healthy eyes in 3D imaging such as MRI or computed tomography (CT). For example, McCaffery et al proposed a parametrical model (7) for a coarse segmentation of each different eye structure (eg, lens or VH). Other approaches include the 3D measurement of shape of the retina to study abnormal shape changes and peripheral vision (8) or the construction of 3D meshes in MRI with morphologic parameters such as distance from the posterior corneal pole and deviation from sphericity (9) However, owing to the lack of statistical information extracted from the variability of a population, the previously mentioned parametric models are often inconsistent with the pathology of ocular MRI, especially for UM patients wherein motion and bias field artifacts in MRI acquisition can be observed.

Our previous work provided a framework (10) to automatically segment the pediatric eye from MRIs based on a 3D active shape model (ASM) (11). This model captures

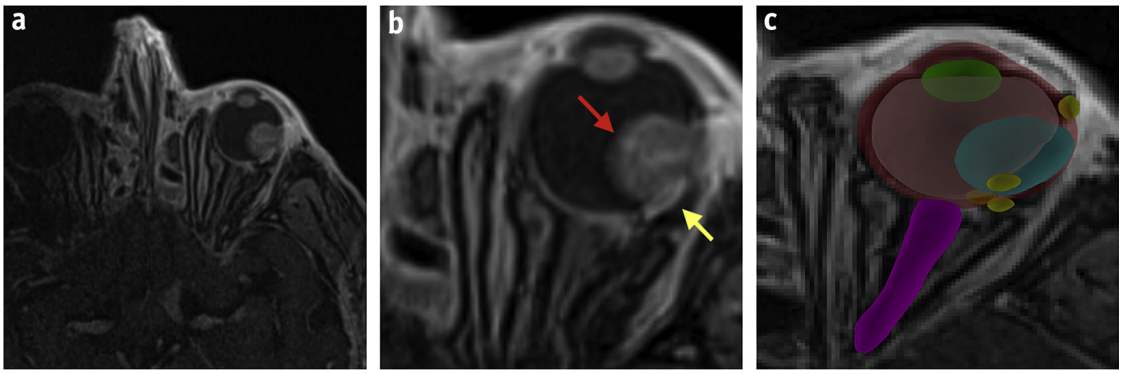

Fig. 1. An example of a T1-weighted vibe magnetic resonance image of a patient with uveal melanoma (UM) to demonstrate the challenge of 3D UM eye model construction (with the presence of motion and tumors with hemorrhage and tantalum clips). (a) Example of whole magnetic resonance image. (b) Example of cropping image with the motion (yellow arrow) and the tumor (red arrow), and (c) Example 3D UM patient-specific eye model. (A color version of this figure is available at https://doi.org/10.1016/j.ijrobp.2018.05.004.)

both the shape of deformation of structures and the intensity variations. It was applied to segment different structures (the CS, VH, and lens) in T1-weighted 3T MR images of healthy and asleep children's eyes. In this work, we reproduced this image processing schema for awake adult eyes in which more challenges such as motion and bias field artifacts can be observed. It should be noted that the lower clinical field-strengths (1.5T) MRI acquisition is more difficult for the measurement of the UM tumors and eye structures dimensions than other high-field (3T or 7T) ocular MRI (12). The higher tesla MR images with high resolution can minimize the motion images of the eye in which the tumor and surrounding tissues can clearly be discriminated. This work is the first step toward building a 3D patient-specific eye model with the presence of tumors and clips that would help reduce unnecessary radiation of normal ocular structures in PT treatment. We have simplified the eye model that could be further improved by the inclusion of other structures such as the ciliary body, macula, retina, and cornea. Note, however, that the macula, the retina, and the border between the sclera and the cornea are not clearly visible in T1-weighted MR images at 1.5T. In this article, we considered the lens, VH, optic-nerve, and CS. It should also be noted that there is no obstacle to extending the segmentation method for the ciliary body and the anterior chamber. The optic disc can be extracted from the intersection of the CS and optic nerve. The separation of cornea and sclera from the CS structure can be inferred by using their neighboring structures, that is, a cut of CS to obtain the whole of ciliary body, lens, and anterior chamber will contain the cornea.

Methods and Materials

Clinical dataset

Our study contains images of 30 healthy eyes from 16 volunteers, ranging in age from 23 to 46 years with a mean of 29 $\pm$ 5.4 years and 7 eyes from UM patients aged 63 $\pm$ 14 years (range 36-74). All subjects gave written informed consent before participation. Cohort median eye size is 24.9 mm of diameter (range 23-26.5). All MRI examinations were performed on a large-bore 1.5T MRI system (Siemens Magnetom Aera, Erlangen, Germany) using a surface coil of 7 cm. T1-weighted 3D volume interpolated gradient echo MR images were acquired with the following acquisition parameters: repetition time 6.55 ms; echo time 2.39

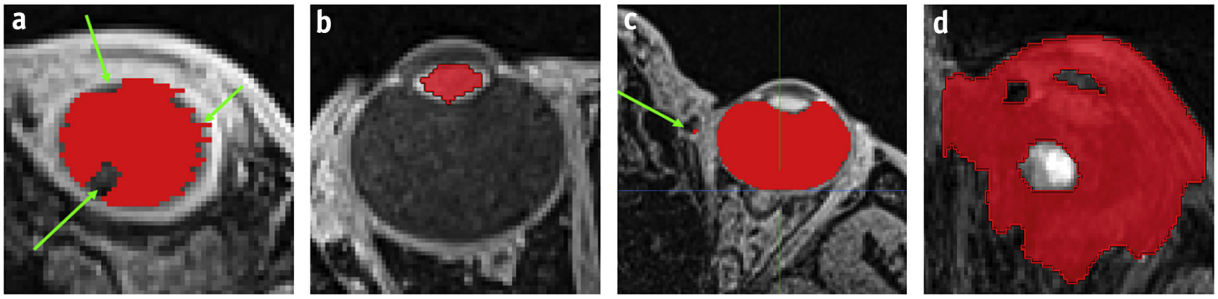

Fig. 2. Different challenges of manual uveal melanoma eye anatomy delineations in magnetic resonance imaging. The border of the vitreous humor (VH) (a) and of the lens (b) cannot be correctly segmented in some slices; (c) a small, noisy object with the same image characteristic of the VH located outside (green arrow); (d) because of the big tumor, the VH with poor contrast cannot be segmented. (A color version of this figure is available at https://doi.org/10.1016/j.ijrobp.2018.05.004.)

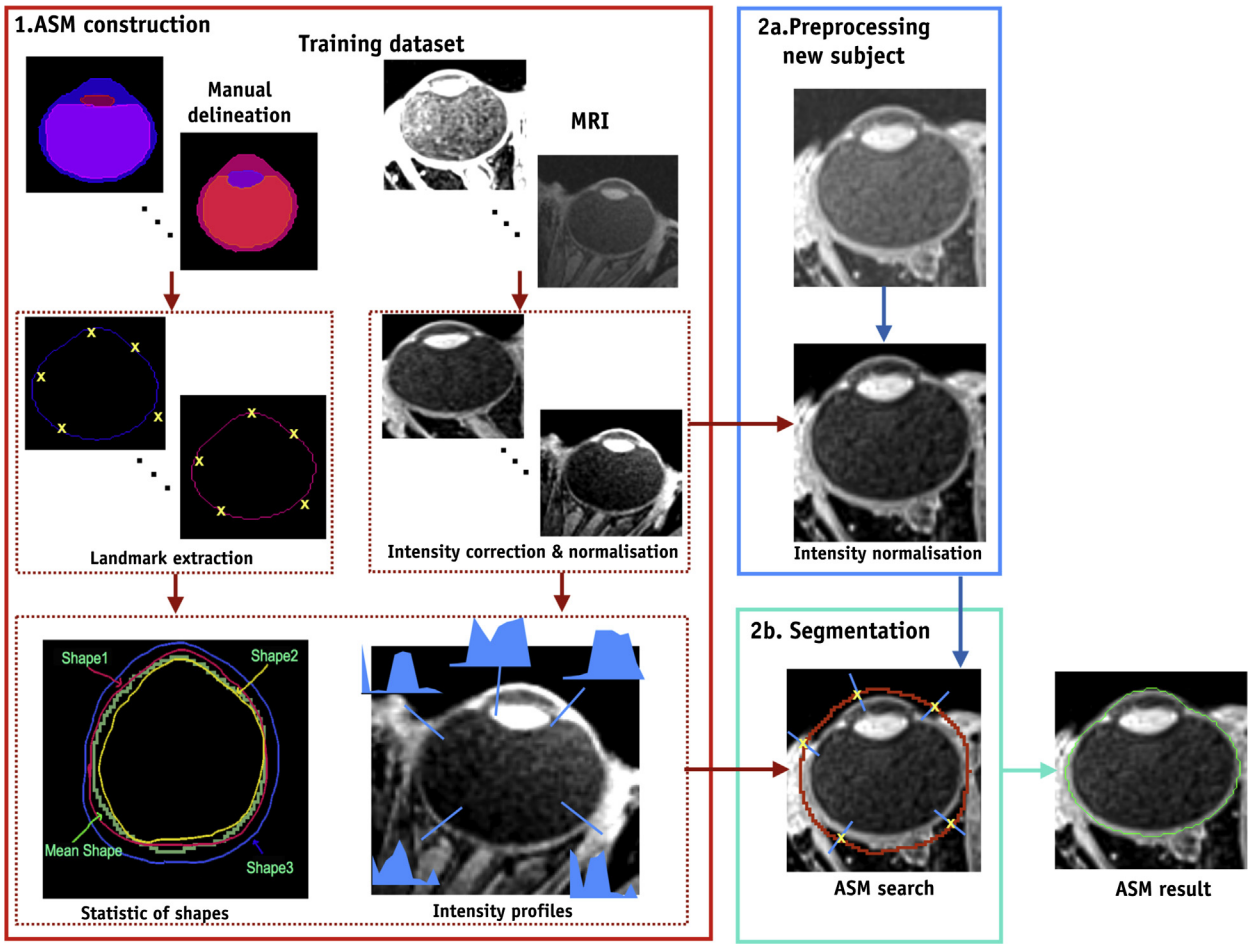

Fig. 3. Main pipeline of our proposed active shape model applied to an adult ocular magnetic resonance imaging dataset.

ms; flip angle 120; voxel size 0.5 × 0.5 × 0.5 mm^3; gap 20% and dimension 256 × 256 × 80. The volunteers received an MR image without contrast, and the patients received the MR image with and without contrast.

Special care was taken to position the surface coil above the eye to avoid an asymmetric signal reduction from the center to the periphery of the acquisition field. Subjects were instructed to fix their gaze on a spot centered in the middle of the scanner during acquisition. Acquisition time was around 4 minutes per sequence, and native acquisition direction was transversal, with middle slice defined as the plane that goes through the pupil center and optical nerve insertion and field center placed just before the optical nerve head.

Manual segmentation

In order to train and validate our method, manual delineations of the lens, VH, CS, and optic nerve were done by one senior radiation oncologist in our institution using the radiation therapy planning software Velocity (Varian Medical System, Palo Alto, CA). This procedure is done in a semisupervised way. First, the expert set the intensity value to choose the best fit candidate for the CS and VH. Then, manual editing was done to refine borders and remove outlier regions. Manual segmentations of the lens and optic nerve were performed by direct delineation of the border using a stylus.

Method

The input of this study is a DICOM-RT dataset that includes both MR images and manual segmentations of anatomic structures of the eye. Our proposed scheme consists of extracting, training, and generating 2 pieces of information: intensity profiles and shape statistics. Figure 3 shows the main pipeline of our proposed ASM model applied to an adult ocular MRI dataset. In the following subsection, we describe in detail the creation of intensity profile, the estimation of shape statistic from the training dataset, and how to segment a new subject.

Intensity profile generation

Manual delineations are used to define a volume of interest (VOI) in the eye from the whole MR image. In practice, we

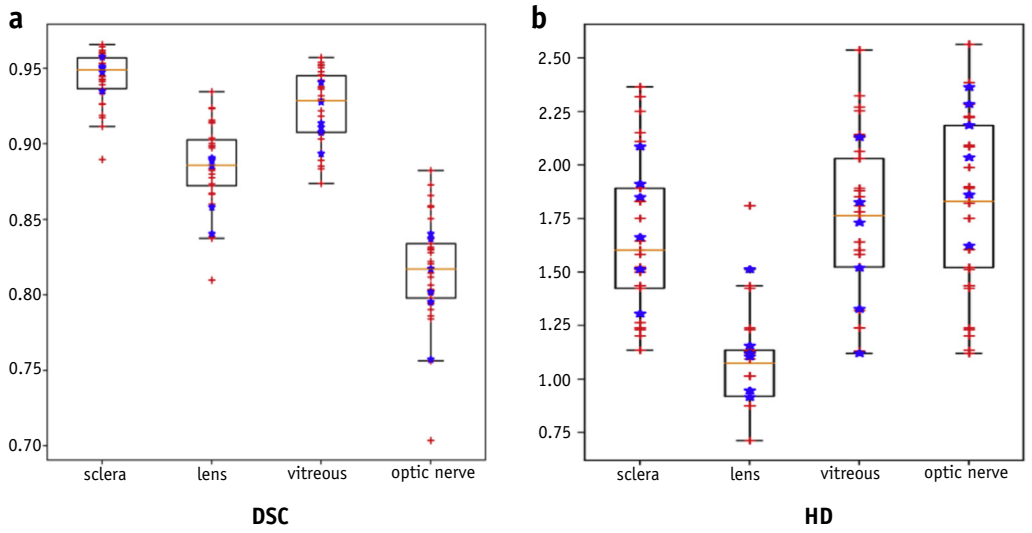

Fig. 4. Percentage of overlap using (a) the Dice similarity coefficient (DSC) value and (b) the Hausdorff distance (HD) (in mm) of volunteer eyes (red+) and patient eyes (blue*) compared with manual segmentation. (A color version of this figure is available at https://doi.org/10.1016/j.ijrobp.2018.05.004.)

expand the VOI to 22.5 mm in each orthogonal direction from its center to make sure that the optic nerve is always included (ie, a $45 \times 45 \times 45$ mm^3 volume; see Fig. 1b). For a new subject, the center of the eye can be either manually determined (mouse-click) or automatically estimated by using the fast radial symmetry algorithm (13). MR image quality is affected by many factors, such as noise, low varying intensity, variations due to nonuniform magnetic fields, imperfections of coils, and magnetic susceptibility at interfaces, and can be influenced by different parameters such as signal-to-noise ratio or acquisition time. Therefore, the intensities are not uniform throughout our training MRI dataset. To compensate for such effects, we processed the MRI volumes with an anisotropic diffusion filter (14), which reduces noise without removing significant image content. Then, we applied the N4 algorithm (15) to correct the bias field variations of MRI and histogram-based intensities normalization (16) to build an intensity profile over the training dataset.

Statistical shape modeling

We represented manually segmented eye surfaces as a point cloud by using a mesh construction. We then selected an even distribution of points over the surface of each structure. To build a standard landmark for the ASM, we fixed the number of points for each type of eye structures: 400 points for the lens, 1000 points for the optic nerve, and 2000 points for the CS and the VH. Rigid registration (17) was applied to find the optimal rotation and translation between corresponding 3D point clouds throughout the training dataset. We then applied a nonrigid registration algorithm (18) to recover the spatial transformation of these point clouds.

Once the landmark points of surface were extracted and aligned, the principal components were computed in order to describe the observed variation under a simpler and smaller dimension. Then, a constrained model-based algorithm that can take into account the shape's deformation from the variability of a population is used to form the basis of a statistical shape information. ASMs proposed by Cootes et al (11) are certainly among the most popular statistical shape models (19). It has been applied to numerous image segmentation applications. ASMs define a point distribution model x by the transformation T and the vector of shape parameters b as follows:

$$x \approx T(\overline{x} + \Phi b) \quad (1)$$

where x is the mean shape and $\Phi = (\phi_1, \phi_2, \ldots . \phi_n)$ is the matrix of eigenvectors corresponding to the variation of the model at each point. The shape model is constrained within the range of training shapes by modifying the bi value under the constraints $\pm 3\sqrt{\lambda_i}, i = 1 \ldots n$; λ is the eigenvalue corresponding to the matrix Φ. Shape adjustments are calculated by updating the transformation T and shape parameters b to better fit the current x onto the set of points given by $x + dx$.

Automated segmentation of a new subject

After training, automated segmentation of a new subject is carried out. The subject MR image is cropped using a VOI centered on the eye and of the same size as in the training set ($45 \times 45 \times 45$ mm^3). The same preprocessing pipeline as in the training case is applied to improve the quality of the MR image and to normalize the intensity with anisotropic diffusion denoising, bias field correction, and histogram equalization. The shapes of CS, VH, lens, and optic nerve are independently generated using the statistical shape information of the

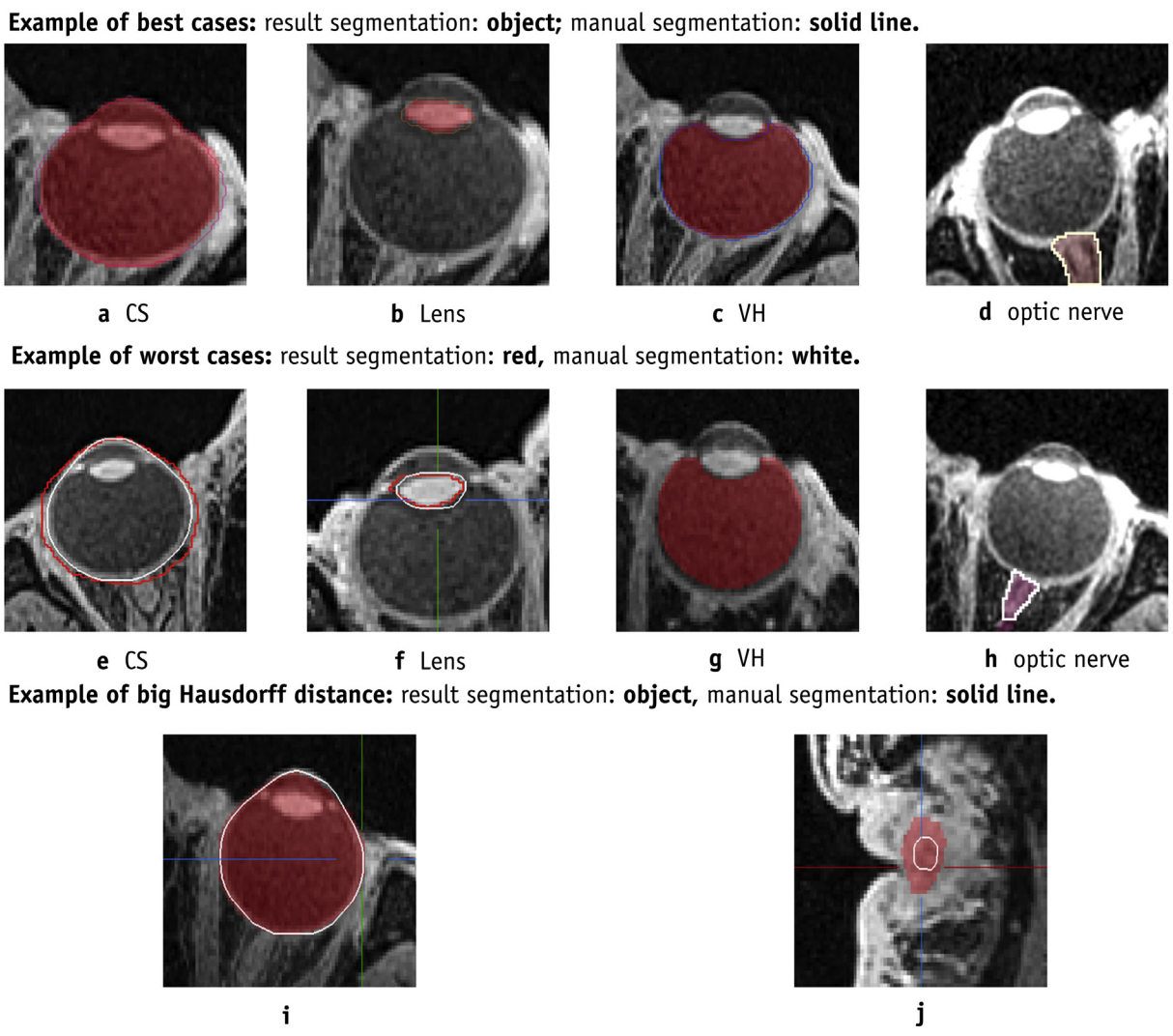

Fig. 5. Examples of automated segmentation for the sclera (SC), lens, vitreous humor (VH), and optic nerve: The first row shows the best segmentation cases (a-d); the second row shows some worst cases (e-h); the last row shows an example of big Hausdorff distance values observed at the end of the object (j), although the good segmentation was obtained with the rest of the object.

training dataset. Considering each landmark point of shapes, the intensity perpendicular to the surfaces (11 voxels for the CS and the VH, and 7 voxels for the lens and the optic nerve) is compared with the intensity profiles provided by the ASM using Mahalanobis distance. The new matched shape is constructed minimizing this distance at all landmark points. The average calculation time for each testing eye structure was 10 s using a Core i5 computer with 8 GB of memory. An open source implementation in Python will be made available. It allows DICOM-RT format as input and produces the segmentation output with different common medical image file formats, for example, point cloud (VTK), binary file (.hdr, .nii), and the like.

Evaluation tools

We performed a leave-one-out cross-validation to quantitatively compare the results of the proposed segmentation approach and ocular adult MRI data (mixing both volunteers and UM patients), that is, we iteratively chose 1 observation from all data as a validation subject and its manual segmentation as the ground truth, while the remaining subjects were considered for the training set. The quality of the segmentations was evaluated by computing the volume overlap using the Dice similarity coefficient (DSC; see Equation 2) and the contour distance using the Hausdorff distance (HD; see Equation 3).

$$DSC = \frac{2|S \cap G|}{|S| + |G|} \tag{2}$$

$$HD(S,G) = max\left\{ \underset{s \in S}{sup} \underset{g \in G}{inf} d(s,g), \underset{g \in G}{sup} \underset{s \in S}{inf} d(s,g) \right\} \tag{3}$$

where S is the segmentation result, G is the ground truth and *sup* (respectively *inf*) represents the *supremum* (the *infimum*).

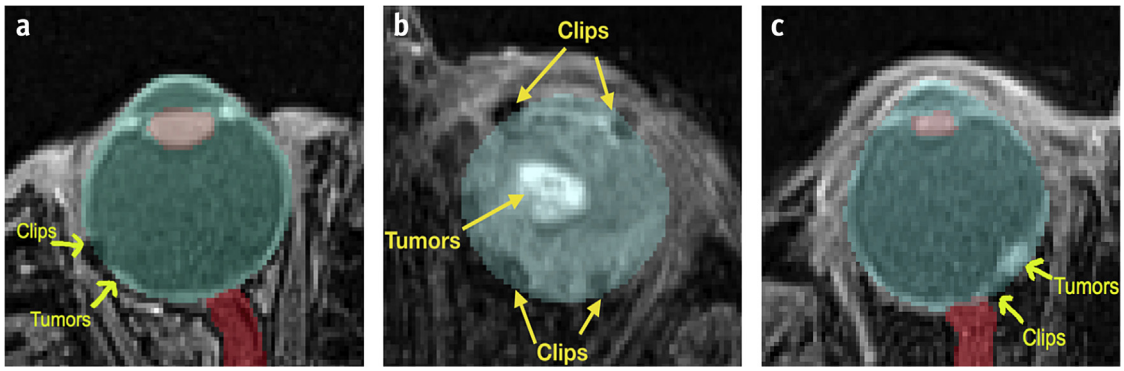

Fig. 6. An example of automated segmentation results of the sclera with the presence of a uveal melanoma tumor and clips (a-c).

Results

Results are presented as boxplots in Figure 4. The midline of the box represents the median, bounding boxes are constructed from the 25th and 75th percentile, and whiskers are showing minimum and maximum of the distribution. Figure 4a shows the result of DSC measurement. The median of the DSC was 94.5 ± 1.6% for the CS, 92.2 ± 2.4% for the VH, 88.3 ± 2.8% for the lens, and 81.9 ± 3.4% for the optic nerve. High volume overlap values were obtained for the segmentation of both the CS and the VH, similar to previously reported results for the child study (10). The DSC values of small objects located nearby muscles (such as lens and optic nerve; Fig. 5f and 5h) were less optimal compared to the CS or the VH. Some outliers (or other big errors in overlap) can be identified as they are related to the biggest or smallest eyes used as validation subjects according to each corresponding set of training data (Fig. 5e and 5g). Recall that the DSC is sensitive to small structures, that is, 1 missed voxel of thin structure will have a stronger penalty than in a larger structure (20). Because previously reported MRI segmentation results for the lens or optic nerve were rare, we refer to the reported DSC values of Fortunati et al (21) in CT images (with 67% for the lens and 62% for the optic nerve) and of Deeley et al (20) in combining CT and MR images (with 60% for the optic nerve). They also reported an interexpert delineation for the optic nerve with the DSC lower than 60%. (20) Our segmentation framework achieves 88.3% and 81.9% for lens and optic nerve, respectively.

Figure 4b shows the boxplot of a contour HD measurement. Median HD was of 1.64 ± 0.35 mm (≈ 3.28 voxels) for the CS, 1.73 ± 0.36 mm (≈ 3.46 voxels) for the VH, 1.09 ± 0.2 mm (≈ 2.18 voxels) for the lens and 1.86 ± 0.4 mm (≈ 3.72 voxels) for the optic nerve. The lens presents the best accuracy in terms of the HD measurement, while its slightly lower DSC is explained by its small size. In this experiment, results for optic nerve regions of interest delineation were less optimal both in terms of the DSC and the HD, because the real shape of the optic nerve presents large variability. This region is also difficult to segment owing to its nearby muscles. The maximum HD value that can be observed in the slices with the end of object is 2.5 mm (≈ 5 voxels) (Fig. 5i). In this region, the variation of the manual segmentation used as input for training is large over each eye subject in training. The HD evaluation of the optic nerve is 1.86 mm versus 6.63 mm as reported in Fortunati et al (21).

In the first row of Figure 6, the accuracy capacity of ASM segmentation to retrieve the real shape of the eye anatomy in MRI with the presence of motion is shown, while the last row also shows that automated ASM segmentation can succeed in UM patients with a large melanoma and 4 clips.

Conclusions

To our knowledge, our work is the first to attempt to automatically segment anatomic adult eye structures with UM. Our results show that automated ASM segmentation can successfully be performed in the presence of motion, tumor, and tantalum clips. It allows for potential improvements in diagnosis, treatment planning, and follow-up monitoring while reducing the time spent by the multidisciplinary ocular oncology teams (ophthalmologists, radiation oncologists, and medical physicists). Our pipeline can be also extended to other ocular magnetic fields 3T or 7T by creating a corresponding training set. Our framework would benefit from the higher spatial resolution and intensity contrast provided at high and ultra-high MR fields (12). However, 7T is not widely available and remains an area of high research focus with clinical use to follow. Further developments are needed for precise segmentation of the tumor and tantalum clips (eg, including other MR contrasts for tumor segmentation or a specific clip ASM model). We will focus our future work on the segmentation of a larger dataset with diversity in eye sizes, based on a combination of datasets from many sites with different acquisition conditions (include mixed adult-children eyes) or imaging multimodalities.

References

1. Lemke A, Hosten N, Bomfeld N, et al. Uveal melanoma: Correlation of histopathologic and radiologic findings by using thin-section MR imaging with a surface coil. *Radiology* 1999;210: 775-783.
2. Singh A, Bergman L, Seregard S. Uveal melanoma: Epidemiologic aspects. *Ophthalmol Clin North Am* 2005;18:75-84, viii.
3. Egger E, Schalenbourg A, Zografos L, et al. Maximizing local tumor control and survival after proton beam radiotherapy of uveal melanoma. *Int J Radiat Oncol Biol Phys* 2001;51:138-147.
4. Damato B, Kacperek A, Errington D, et al. Proton beam radiotherapy of uveal melanoma. *Saudi J Ophthalmol* 2013;27:151-157.
5. Daftari I, Aghaian E, O'Brien J, et al. 3D MRI-based tumor delineation of ocular melanoma and its comparison with conventional techniques. *Med Phys* 2005;32:3355-3362.
6. Tartaglione T, Pagliara MM, Sciandra M, et al. Uveal melanoma: Evaluation of extrascleral extension using thin-section MR of the eye with surface coils. *Radiol Med* 2014;119:775-783.
7. McCaffery S, Simon E, Fischbein N. Three-dimensional high-resolution magnetic resonance imaging of ocular and orbital malignancies. *Arch Ophthalmol* 2002;120:747-754.
8. Beenakker J, Shamonin D, Webb G, et al. Automated retinal topographic maps measured with magnetic resonance imaging. *Invest Ophthalmol Vis Sci* 2015;56:1033-1039.
9. Singh K, Logan N, Gilmartin B. Three-dimensional modeling of the human eye based on magnetic resonance imaging. *Invest Ophthalmol Vis Sci* 2006;47:2272-2279.
10. Ciller C, De Zanet S, Rüegsegger MB, et al. Automatic segmentation of the eye in 3D magnetic resonance imaging: A novel statistical shape model for treatment planning of retinoblastoma. *Int J Radiat Oncol Biol Phys* 2015;92:794-802.
11. Cootes T, Taylor C, Cooper D. Active shape models — their training and application. *Comput Vis Image Underst* 1995;61:38-59.
12. Beenakker J-W, Ferreira TA, Soemarwoto KP, et al. Clinical evaluation of ultra-high-field MRI for three-dimensional visualisation of tumour size in uveal melanoma patients, with direct relevance to treatment planning. *MAGMA* 2016;29:571-577.
13. De Zanet S, Ciller C, Rudolph T. Landmark detection for fusion of fundus and MRI toward a patient-specific multimodal eye model. *IEEE Trans Biomed Eng* 2015;62:532-540.
14. Perona P, Malik P. Scale-space and edge detection using anisotropic diffusion. *IEEE Trans Pattern Anal Mach Intell* 1990;12:629-639.
15. Tustison N, Avants BB, Cook PA, et al. N4itk: Improved n3 bias correction. *IEEE Trans Med Imaging* 2010;29:1310-1320.
16. Nyu L, Udupa J, Zhang X. New variants of a method of MRI scale standardization. *IEEE Trans Med Imaging* 2000;19:143-150.
17. Besl P, McKay N. A method for registration of 3-D shapes. *IEEE Trans Pattern Anal Mach Intell* 1992;14:239-256.
18. Myronenko A, Song S. Point set registration: Coherent point drift. *IEEE Trans Pattern Anal Mach Intell* 2010;32:2262-2275.
19. Heimann T, Meinzer H. Statistical shape models for 3d medical image segmentation: A review. *Med Image Anal* 2009;13:543-563.
20. Deeley M, Chen A, Datteri R, et al. Comparison of manual and automatic segmentation methods for brain structures in the presence of space-occupying lesions: A multi-expert study. *Phys Med Biol* 2011; 56:4557-4577.
21. Fortunati V, Verhaart RF, van der Lijn F, et al. Tissue segmentation of head and neck CT images for treatment planning: A multiatlas approach combined with intensity modeling. *Med Phys* 2013;40: 071905.